

---

# Impact of Voxel Normalization on Machine Learning-Based Method: A Study on Pulmonary Nodule Malignancy Diagnosis Using Low-Dose Computed Tomography (LDCT)

---

Chia-Chi Hsiao , [Chen-Hao Peng](#) , [Fu-Zong Wu](#) \* , [Da-Chuan Cheng](#) \*

Posted Date: 23 October 2023

doi: 10.20944/preprints202310.1378.v1

Keywords: lung cancer; isotropic voxel reconstruction; lung nodule classification; radiomics; computer-aided diagnosis



Preprints.org is a free multidiscipline platform providing preprint service that is dedicated to making early versions of research outputs permanently available and citable. Preprints posted at Preprints.org appear in Web of Science, Crossref, Google Scholar, Scilit, Europe PMC.

Copyright: This is an open access article distributed under the Creative Commons Attribution License which permits unrestricted use, distribution, and reproduction in any medium, provided the original work is properly cited.

Article

# Impact of Voxel Normalization on Machine Learning-Based Method: A Study on Pulmonary Nodule Malignancy Diagnosis Using Low-Dose Computed Tomography (LDCT)

Chia-Chi Hsiao <sup>1</sup>, Chen-Hao Peng <sup>2</sup>, Fu-Zong Wu <sup>1,\*</sup>,† and Da-Chuan Cheng <sup>2,\*</sup>

<sup>1</sup> Department of Radiology, Kaohsiung Veterans, General Hospital, Kaohsiung City, Taiwan, ROC; vghkscchsiao1@gmail.com

<sup>2</sup> Department of Biomedical Imaging and Radiological Science, China Medical University, Taichung 404, Taiwan

\* Correspondence: dccheng@mail.cmu.edu.tw (D.C.C.); cmvwu1029@gmail.com (F.Z.W.)

† These authors contributed equally to this work and should be considered co-corresponding authors.

**Abstract:** Lung cancer (LC) stands as the foremost cause of cancer-related fatality rates worldwide. Early diagnosis significantly enhances patient survival rate. Nowadays, low dose computed tomography (LDCT) is widely employed on chest as a tool for large-scale lung cancer screening. Nonetheless, a large amount of chest radiographs causes an onerous burden on radiologists. Some computer-aided diagnostic (CAD) tools can provide insights to medical images for diagnosis and augmenting diagnostic speed. However, due to variation in parameter settings across different patients, substantial discrepancies in image voxels persist. We find different voxel-size causing a compromise between model generalization and diagnostic efficacy. This study investigates the performance disparities of diagnostic models trained on original images and LDCT images reconstructed to different voxel-sizes but isotropic. The application is to differentiate a nodule to be benign or malignant. Using 11 features, a support vector machine (SVM) is trained on LDCT images with an isotropic voxel having side-length of 1.5 mm for 225 patients in house. The result yields a favorable model performance with an accuracy of 0.9596 and an area under the receiver operating characteristic curve (ROC/AUC) of 0.9855. In addition to furnish CAD tools for clinical applications, future research is encouraged to include LDCT images from multi-centers.

**Keywords:** lung cancer; isotropic voxel reconstruction; lung nodule classification; radiomics; computer-aided diagnosis

## 1. Introduction

According to the 2023 World Cancer Statistics[1], although the overall mortality rate of lung cancer (LC) has shown a decline in 2023 compared to previous years, it remains the second most prevalent cancer globally in terms of both overall cancer-related deaths and new cases. Approximately 230,000 individuals are newly diagnosed with LC each year globally, and among them about 120,000 suffer to malignancy. Clinically, LC can be roughly classified into non-small cell lung cancer (NSCLC) and small cell lung cancer (SCLC). NSCLC is the majority which accounts for approximately 85% of LC cases [2], and can further be categorized into adenocarcinoma and squamous cell carcinoma subtypes [3]. Early detection and treatment of NSCLC typically lead to better prognoses and higher five-year survival rates [3].

Current facility for early LC screening is primarily involved with low-dose computed tomography (LDCT), enabling rapid and large-scale diagnosis on individuals having high risk factors [4]. However, these screenings generate a large amount of images that require interpretation by radiologists. This not only results in a substantial burden on human resources but also introduces variations in experience and subjective awareness among different radiologists, lacking unified

diagnostic criteria [5]. Within LDCT images, pulmonary nodules (PNs) represent areas suspected of being lesions and can be preliminarily categorized into three types: solid nodules (SN), part-solid nodules (PSN), and ground glass nodules (GGN) [6]. Typically, radiologists rely on visible characteristics such as PNs size, edge shape, and nodule pattern for diagnosis [7], such as Lung-RADS™ [8]. However, this approach often yields a high rate of false positives [9], ultimately needing a pathological biopsy for a final confirmation. This process often causes patients to have unnecessary and invasive risks [10]. Figure 1 illustrates PNs, where benign and malignant nodules appear strikingly similar to our eyes, rendering precise diagnoses challenging.

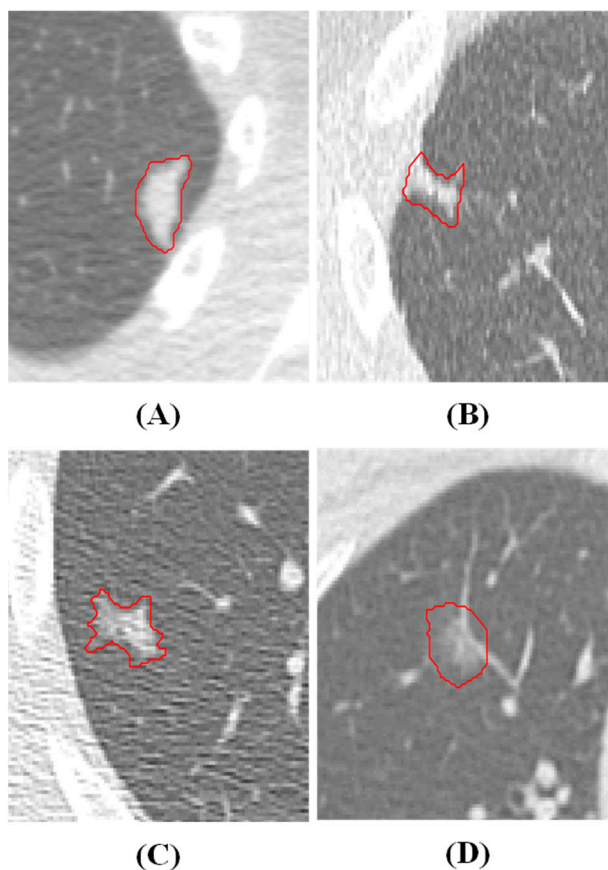


**Figure 1.** PNs Presentation. (A) and (B) depict benign PNs, while (C) and (D) show malignant PNs.

Using machine learning (ML) and deep learning (DL) onto pulmonary nodule detection and diagnosis in chest CT images have been studied since decades. Especially, radiomics [11] is a feature extraction technique usually combined with classifiers to establish models, which are able to provide physicians with an alternative opinion beyond visible characteristics. Previous study indicates that such models significantly enhance reading speed and diagnostic precision for physicians [12]. Numerous studies focus on PN detection and classification can achieve promising results [13-23]. For example, Kumar et al. [16] propose an approach utilizing autoencoders to extract features from raw images and employ a decision tree for binary classification, which achieves an accuracy of 0.7501. Shen et al. [22] introduce a method using multi-scale convolutional neural networks (MCNN) to distinguish PN's malignancy, capturing different-sized patches of each PN and simultaneously using convolutional neural networks (CNN) for discrimination, which achieves an accuracy of 0.8612 on the LIDC-IDRI dataset [5]. Mehta et al. [19] in 2021 present a model that utilizes 3D CNNs in combination with volumetric radiomics and imaging biomarkers to diagnose PNs malignancy. By incorporating 3D PNs images, radiomics, and LIDC-IDRI biomarkers, they achieve an ROC/AUC of 0.8659. In 2021, Lu et al. [18] introduce a method that integrated the Marine Predators Algorithm with CNN for the diagnosis of PNs. This approach achieves an impressive performance with an accuracy

of 0.934 and a sensitivity of 0.984. Halder et al. [24] attain the best PNs diagnostic model performance using the LIDC-IDRI dataset in 2021. They employ morphology and two CNN networks, achieving an accuracy of 0.9610 and an AUC of 0.9936.

However, above mentioned studies face some common challenges. First, most patients in LIDC-IDRI dataset lack pathological biopsy results on nodule malignancy diagnosis, which are considered to be gold standard. LIDC-IDRI provides suspicion scores of nodule malignancy, ranging from 1 to 5 made by radiologists. Most previous studies classify nodules with scores of 1 and 2 as benign and those with scores of 4 and 5 as malignant, however, the actual malignancy of PNs remains uncertain. Second, previous studies typically use raw LDCT images as inputs to their models. They ignore a fact that images undergoing LDCT imaging may have different modality settings such as pixel spacing (PS) and slice thickness (SK). This ignorance results in a question whether the uniformity on voxel-size would affect model diagnostic performance or not. For instance, Kim et al. [25] in 2019 review factors that could impact the quantification of CT image features, highlighting the significant influence of PS and SK on feature quantification. Most features demonstrate different impacts before and after normalization on PS and SK. Lu et al. [26] in 2017 improve model diagnostic performance by reconstructing positron emission tomography (PET) images into uniform voxel-size. Through investigating the impacts of different voxel-sizes on PET image quantification or diagnosis, their study offers valuable insights. Above mentioned studies focus on traditional machine learning method, therefore they can examine feature impact accordingly. Recent studies often use neural networks (NN) and deep learning such as [27], which is out of this study scope. This study is motivated by above mentioned problems so that we do not consider using NN and DL. Furthermore, DL models demand large dataset for training, which is not suitable to our small dataset in this study.

## 2. Materials and Methods

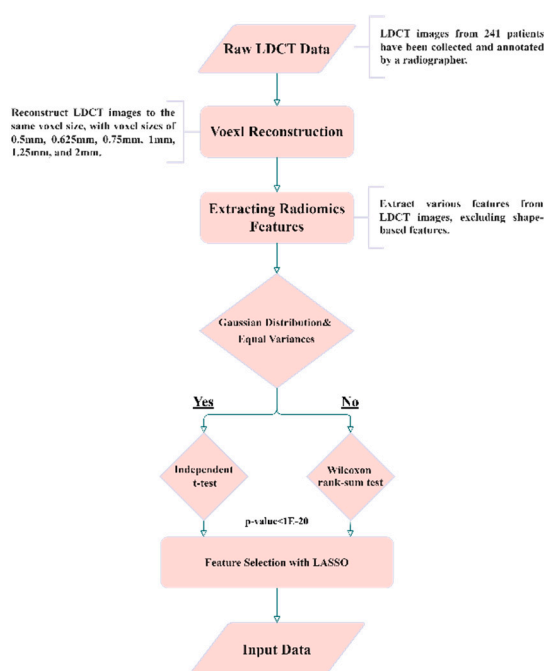


**Figure 2.** Experimental flowchart of this study.

### *Dataset in House and Annotation*

LDCT image data are collected from Kaohsiung Veterans General Hospital (KVGH), including 160 malignant and 81 benign PNs from a total of 241 patients. The data collection process has been approved by the Institutional Review Board (IRB) of KVGH with the IRB number VGHKS18-CT5-09. The malignancy status of each PN is defined by pathological biopsy and the boundary of PN is annotated by an experienced radiological technician. LifeX (Version 6.2.0, C. Nioche, Inserm, France)

is open-source software that was first published in the year 2018 [28]. Its application involves reading DICOM images and synchronizing the display and annotation of medical images in coronal, sagittal, and axial slices. It also concurrently supports users in the extraction of radiomics features within regions of interest (ROIs). We use LifeX as annotation tool, and we can output nearly raw raster data (NRRD) format for image feature extraction. However, due to technical problems of LifeX, 3 benign and 13 malignant patients in which ROI annotations result in errors. Therefore, these 16 patient data are excluded for following process. The final images (for following training and test usage) have either a size of 512×512 or 768×768 depending on the raw data. Notably, the radiomics features are extracted only in ROIs in the reconstructed images, not directly from LDCT raw images.

#### *Isotropic Voxel Normalization and Image Reconstruction*

To explore the reproducibility and model performance of PN malignancy diagnosis using ML method, we normalize PS and ST of all LDCT images using bicubic interpolation. This reconstruction aims to achieve consistent spatial resolution across all LDCT images, making them isotropic in three axes. Furthermore, to evaluate the influence of different voxel sizes and spatial resolutions on the model and features, we reconstruct all images to various voxel-sizes, including 0.5, 0.625, 0.75, 1, 1.25, 1.5, 1.75, and 2 (mm) of side length.

#### *Radiomics and Feature Selection*

We employ radiomics to extract 2112 features from the PN regions of the reconstructed images. Radiomics encompass various quantitative image feature extraction methods, including first-order statistics, shape-based, and texture-based methods [11]. Not all extracted features contribute significantly to PNs malignancy diagnosis, therefore, feature selection is necessary and crucial. Given that PN malignancy is often related to its size [10], we intentionally exclude features with size information. Before feature dimension reduction, in total 14 features related to shape and size are manually excluded (see Table 5 in Appendix A). Moreover, 123 features with identical feature values having no discriminability are also manually excluded. The remaining 1975 features undergo further feature dimension reduction in the following paragraph.

In order to reduce the number of input features for our model, we utilize different methods. First, we utilize the independent t-test [29] and the Wilcoxon rank-sum [30] test to examine significant features for differentiating benign and malignant nodule. To apply the independent t-test, some prerequisites are needed including a normal distribution on a certain feature and modulating equal variance to that distribution. Meeting these prerequisites is crucial for using the independent t-test. Therefore, we first examine normality tests [31] and Levene tests [32] to assess the equality of variances and the type of distribution for both benign and malignant pulmonary nodule groups. If data meet the criteria of a normal distribution and equal variance, we then proceed using independent t-tests for analysis, otherwise, we employ the Wilcoxon rank-sum test for getting p-values. Features with p-values between two classes less than  $10^{-20}$  are considered to be significantly different, which means they are good and distinguishable features. Second, we employ well-known LASSO [33] algorithm. LASSO algorithm effectively reduces coefficients to zero for those features having less contribution to classification, thus achieves feature selection. Third, we apply t-distributed stochastic neighbor embedding (t-SNE) [34] for dimension reduction of selected feature combinations to visualize the distribution of patients in two-dimensional space. t-SNE, belonging to manifold learning, achieves dimension reduction and meanwhile preserves local structure of data distribution. This t-SNE can be found for data visualization and dimension reduction in recent publications.

#### *Support Vector Machine (SVM) and Hyperparameter Optimization*

SVM is a classic classifier [35] known from its strong performance in various classification tasks, particularly in dealing with small datasets. It exhibits better generalization ability compared to DL models in dealing with small dataset [36]. In our study, we compare four combinations on feature

selection: 1) all features without exclusion, 2) features with p-value less than  $10^{-20}$ , 3) features selected by LASSO, and 4) features selected by the t-SNE algorithm. Prior inputting all features into the SVM model, we perform Min-Max Normalization on all features to ensure that different features have comparable numeric ranges. This is a basic feature normalization process. In SVM, the choice of kernel function, which determines the decision boundary, is crucial. We employ the Gaussian Radial Basis Function (RBF) kernel function for our SVM model because most feature distributions are normal distribution after feature selection. In ML models, hyperparameter optimization is highly correlated to final model performance. We use Gaussian Bayesian optimization [37] to tune hyperparameters of SVM model to achieve a better performance.

#### *K-Fold Cross-Validation and Model Performance Evaluation*

In order to know model performance, we manipulate data for training and test as follows. We randomly sample 80% of the benign and malignant data as training data, with the remained 20% serves as test data. This sampling and test process is repeated 4000 times. We thus evaluate model's performance on different voxel sizes and feature selection methods using various metrics: Balanced Accuracy, Weighted Sensitivity, Weighted Precision, Weighted F-score, and Weighted AUC. Equation (1)-(5) represent the formula of these metrics. Finally, we conduct 10-fold cross-validation to assess the model performance and plot ROC curves.

$$\text{Balanced Accuracy} = \frac{1}{k} \sum_{i=0}^k \frac{TP_i}{(TP_i + FN_i)} \quad (1)$$

$$\text{Weighted Sensitivity} = \frac{\sum_{i=0}^k w_i \times TP_i}{\sum_{i=0}^k w_i * (TP_i + FN_i)} \quad (2)$$

$$\text{Weighted Precision} = \frac{\sum_{i=0}^k w_i \times TP_i}{\sum_{i=0}^k w_i * (TP_i + FP_i)} \quad (3)$$

$$\text{Weighted F1 score} = \frac{\sum_{i=0}^k w_i \times \left( \frac{2 \times TP_i}{2 \times TP_i + FP_i + FN_i} \right)}{\sum_{i=0}^k w_i} \quad (4)$$

$$\text{One - vs - All AUC} = \frac{\sum_{i=0}^k w_i \times AUC_i}{\sum_{i=0}^k w_i} \quad (5)$$

### **3. Results**

In Figure 3, we demonstrate the distribution of p-values for features extracted at different voxel sizes reconstructed from the raw image data (LDCT). The value started from 0.5, 0.625 to 2 is the side-length of the isotropic voxel in mm. The word 'original' means there is no reconstruction, it is raw LDCT data. The value started from 200, 400 to 1600 is the number of features. We categorize p-value into four groups: less than 0.05, 1E-10, 1E-20, and 1E-28. It is interesting to find from Figure 3, the majority of features has p-values locating in the range: [0.05, 1E-10]. However, p-value in this range is not able to distinguish or to classify. Therefore, the most part features are useless. We also find that features extracted from the original LDCT images without uniform voxel sizes has the least useful features. Here the useful feature we mean the purple part (p-value < 1E-28). This indicates that voxel normalization indeed affects feature extraction. Through this voxel normalization process using image reconstruction, the extracted image features exhibit significant statistical differences between benign and malignant nodules. This result convinces our hypothesis. Notably, features extracted from reconstructed data normalized to 2mm in side-length perform poorly compared to other side-length. We provide Table 1 for exact quantity of features plotted in Figure 3.

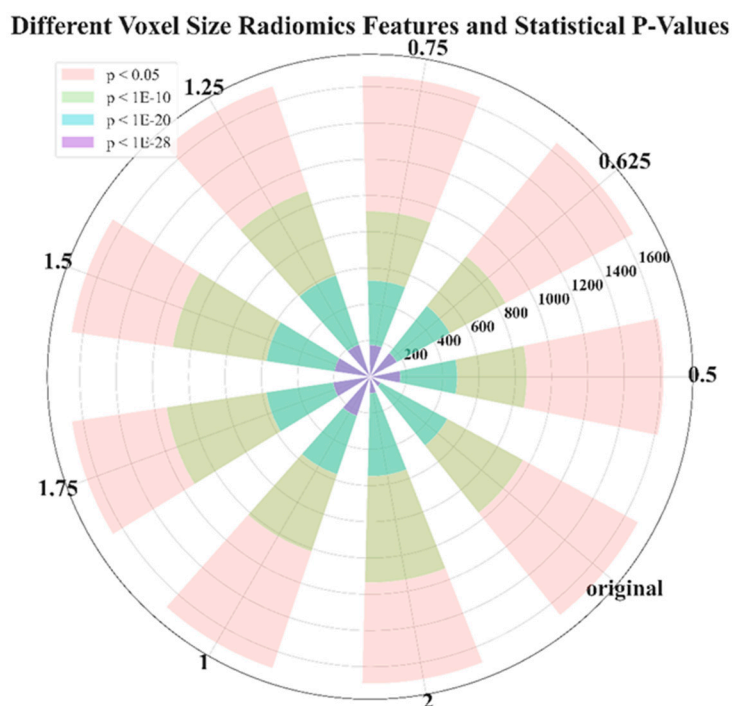


**Figure 3.** p-value distribution of radiomics features extracted from different side-length voxel reconstructed from raw LDCT data. This experiment is to examine the feature efficacy on benign and malignant nodule classification, based on different voxel sizes.

**Table 1.** The quantity of p-value of radiomics features distribution plotted in Figure 3.

VOXEL SIZE	0.5	0.625	0.75	1	1.25	1.5	1.75	2	ORIGINAL
P<0.05	1617	1650	1657	1694	1690	1663	1661	1692	1680
P<1E-10	863	850	913	1016	1081	1100	1134	1135	959
P<1E-20	480	501	531	568	590	578	578	549	485
P<1E-28	166	168	175	227	187	198	206	91	67

In Table 2, we illustrate the number of features before (the baseline) and after feature selection. In Figure 4, we demonstrate the model performance for comparison using 5 metrics illustrated in Equations 1–5. From the result, it shows the best feature selection method is LASSO using only 11 features. Astonished, the second best performance is achieved by reducing the dimensionality of 11 LASSO-selected features to 2 ‘features’ (actually here means 2 directions in the feature space) using t-SNE, resulting in an outstanding performance. The feature distribution on these 2 directions are shown in Figure 7.

**Table 2.** Number of feature after feature selection and raw LDCT images.

	Unfiltered Features	Statistically Filtered Features	LASSO	t-SNE
Feature Number	2061	480	11	2

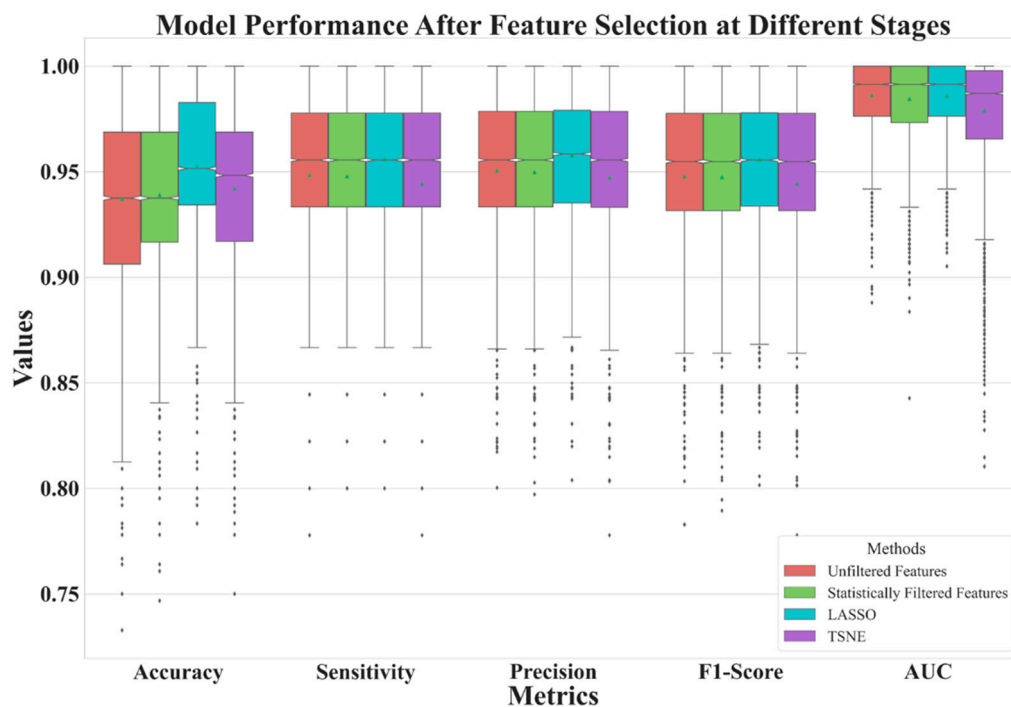


Figure 4. Model performance comparison on three feature selection methods and a baseline.

Figure 5 depicts the performance of features extracted from different voxel sizes reconstruction. We here use LASSO to select features. From the figure, it is obvious to observe that the model has better performances with voxel normalization having side-lengths less than 2 mm. The best model is achieved with features extracted from LDCT images with a side-length of 1.5 mm.

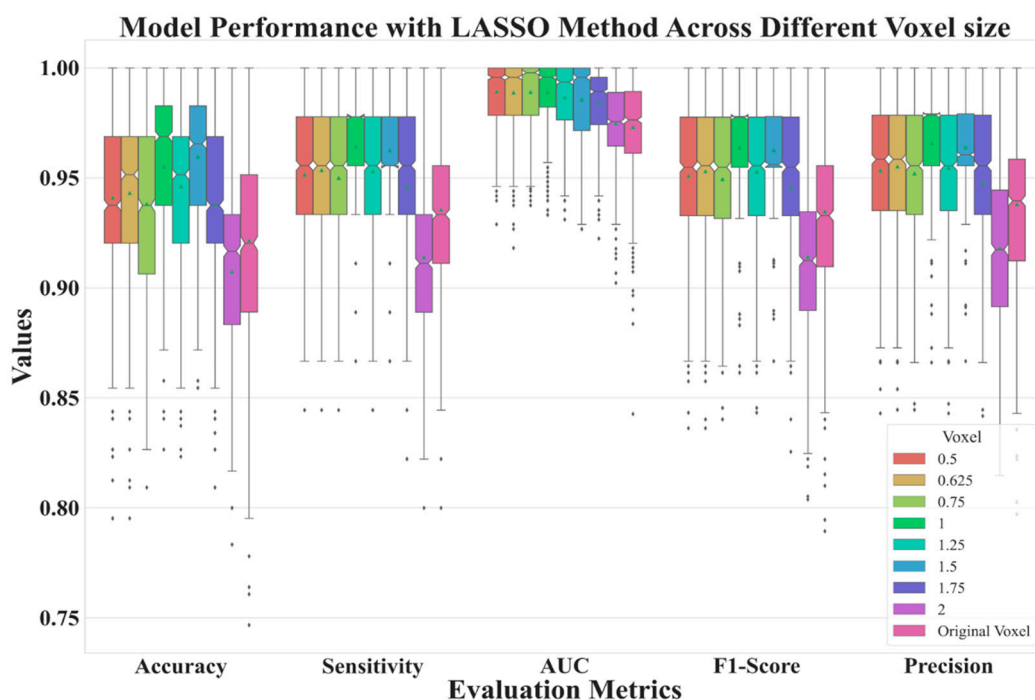
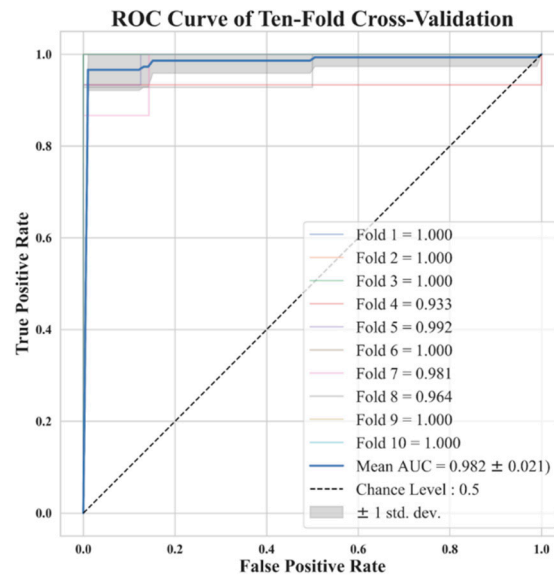


Figure 5. Model performance for reconstructed data with various side-lengths.

In Figure 6, we show ROCs using ten-fold cross-validation with radiomic features selected by LASSO from image reconstruction with a side-length of 1.5 mm. The model average AUC reaches 0.982, indicating a stable diagnostic performance. This is clinically

acceptable for PNs diagnosis. In Figure 7 we demonstrate the distribution on 2D feature space, with two dimension directions. After dimensionality reduction, only 2 features are selected by t-SNE. From this distribution, it is obvious to see that these 11 features are able to effectively classify benign and malignant nodules.



**Figure 6.** Ten-fold cross-validation ROC curve for the model trained with 11 features selected by LASSO with a voxel having a side-length of 1.5 mm.

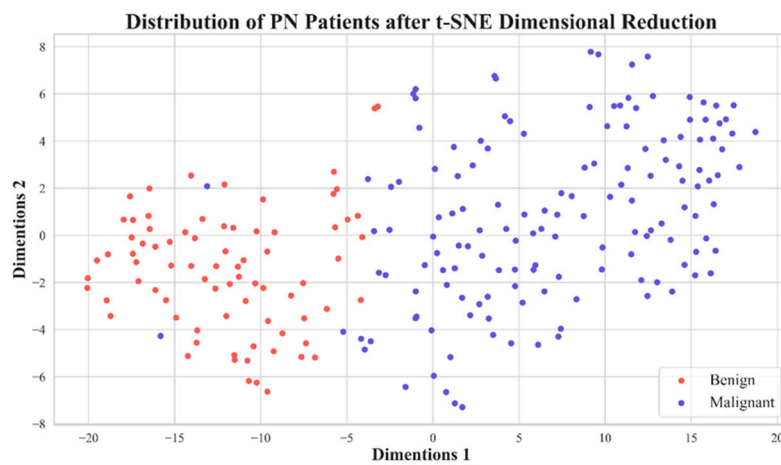


**Figure 7.** Distribution plot of 11 features extracted from PNs with voxel having a side-length of 1.5 mm after dimension reduction using t-SNE.

Finally, Table 3 we compare different results. These results are the averaged values of various metrics in different voxel-size of reconstruction over 4000 times of repetitions. We also compare to state-of-the-art models. Our best result outperforms the most previous methods and is comparable to the best previous study [24]. Besides, deep learning approaches need more time in training than the traditional method.

**Table 3.** Comparison of test results averaged from 4000 times; 80% training and 20% test in partition. The values in the first column denote different side-length of voxel after image reconstruction.

	Accuracy	AUC	Sensitivity	Precision	F1 Score
0.5	0.9409	0.9891	0.9514	0.9533	0.9509
0.625	0.9431	0.9887	0.9535	0.9551	0.9530
0.75	0.9350	0.9890	0.9481	0.9501	0.9473
1	0.9531	0.9890	0.9624	0.9640	0.9620
1.25	0.9467	0.9866	0.9532	0.9548	0.9530
1.5	0.9596	0.9855	0.9619	0.9633	0.9619
1.75	0.9371	0.9844	0.9452	0.9468	0.9449
2	0.9073	0.9747	0.9156	0.9197	0.9159
Original	0.9223	0.9731	0.9357	0.9381	0.9349
Halder et al.2021[24]	0.9610	0.9936	0.9685		
Mehta et al.2021[19]		0.8659			
Shen et al.2017[22]	0.8612				
Lu et al. 2021[18]	0.934	0.984			

#### 4. Discussions

Due to the diversity of patients in clinics and orders from physicians, radiographers use various parameter settings to acquire LDCT images. If these parameter settings are not consistent, it is difficult to compare because of vacancy on baseline. Particularly we mean texture features; different pixel-size on images can cause different results, such as features extracted from Gray Level Co-occurrence Matrix (GLCM), Gray Level Run Length Matrix (GLRLM), Gray Level Size Zone Matrix (GLSZM), and other texture features. Many previous studies have indicated, texture features are crucial for distinguishing the benign and malignant nature of PNs.

Table 4 presents the 11 radiomic features selected by the LASSO in this study. Notably, 7 from the 11 selected features are all texture-related, demonstrating the important role in discriminating benign and malignant PNs. Therefore, voxel normalization is essential and has a profound impact on the reproducibility.

**Table 4.** Description of the 11 Features Utilized by the Model.

Feature Description	Types
original_gldm_SmallDependenceLowGrayLevelEmphasis	Texture
log-sigma-2-0-mm-3D_gldm_DifferenceEntropy	Texture
log-sigma-2-0-mm-3D_gldm_SmallDependenceEmphasis	Texture
log-sigma-3-0-mm-3D_glszm_ZonePercentage	Texture
lbp-2D_gldm_DependenceNonUniformityNormalized	Texture
lbp-3D-m1_gldm_DependenceNonUniformityNormalized	Texture
lbp-3D-m2_gldm_DependenceNonUniformityNormalized	Texture
log-sigma-2-0-mm-3D_firstorder_Mean	First order
lbp-3D-m1_firstorder_Skewness	lbp-3D-First order
wavelet-LLH_firstorder_Mean	First order
wavelet-LHL_firstorder_Mean	First order

In this research, normalizing the voxel size from LDCT images to 1mm-1.5mm yields good model performance. Typically, CT has a spatial resolution ranging from 0.5 mm to 0.625 mm in x-y axis, our collected data fall in the range from 0.6 mm to 0.8 mm. The resolution on z-axis depends on the temporal resolution. Our dataset in house, most images on z-axis resolution fall in the range from 1 mm to 5 mm. We do not have data in z-axis less than 1 mm. The image reconstruction has to consider the spatial and temporal resolution of the raw data, otherwise, it can lead to partial volume effect and subsequently impacts the model performance. Further, reconstructing images with a voxel larger than 1.5 mm on side-length will significantly decrease spatial resolution, making it impossible to

capture fine texture of PNs. Therefore, we recommend that future studies consider voxel reconstruction within the range of 1 mm-1.5 mm, based on a prerequisite that data has higher spatial and temporal resolution than 1 mm in x-y-z axis, i.e.,  $\leq 1$  mm.

One advantage of our study compared to previous researches is that all our patients have pathological diagnoses to confirm the PN's nature, i.e., benign or malignant. This advantage is not present in the large open dataset such as LIDC-IDRI. Research limitations regarding this study are discussed below. This study mainly analyze Asian ethnic groups, and most malignant lesions are adenocarcinoma spectrum. Therefore, the predictive ability for other pathological types of lung cancer may be lower. Particularly, this study mainly distinguishes lung adenocarcinoma spectrum lesions from other benign lesions. Therefore, there is no further study and analysis on the clinical management of these nodules.

## 5. Conclusion

This study uses a ML method combined with radiomic features extracted from reconstructed images with voxel normalization from LDCT. We mainly explore the impact of voxel normalization to prediction performance between benign and malignant pulmonary nodules. Our study offers a recommendation: before using radiomics, the voxel normalization is important and crucial to texture-related studies. The reconstruction has to consider the limitation on raw data temporal resolution.

**Author Contributions:** Conceptualization, D.-C.C.; methodology, D.-C.C., C.-H.P.; software, C.-H.P.; validation, C.-H.P.; formal analysis, D.-C.C. and C.-H.P.; investigation, D.-C.C. and C.-H.P.; resources, F.-Z.W.; data curation, C.-C.H.; writing—original draft preparation, D.-C.C. and C.-H.P.; writing—review and editing, D.-C.C. and F.-Z.W.; visualization, C.-H.P.; supervision, D.-C.C.; project administration, D.-C.C.; funding acquisition, C.-C.H. All authors have read and agreed to the published version of the manuscript.

**Funding:** This research was funded by Kaohsiung Veterans General Hospital, grant number KSVG112-110.

**Institutional Review Board Statement:** The study was conducted in accordance with the Declaration of Helsinki, and approved by the Institutional Review Board (IRB) of KVGH with the IRB number VGHKS18-CT5-09 (protocol code:18-CT5-09, April 3, 2018).

**Informed Consent Statement:** Not applicable.

**Acknowledgments:** In this section, you can acknowledge any support given which is not covered by the author contribution or funding sections.

**Conflicts of Interest:** The authors declare no conflict of interest.

## Appendix A

**Table A1.** Description of the 14 manually excluded features.

Feature Description	Types
original_shape_Elongation	Shape-Based
original_shape_Flatness	Shape-Based
original_shape_LeastAxisLength	Shape-Based
original_shape_MajorAxisLength	Shape-Based
original_shape_Maximum2DDiameterColumn	Shape-Based
original_shape_Maximum2DDiameterRow	Shape-Based
original_shape_Maximum2DDiameterSlice	Shape-Based
original_shape_Maximum3DDiameter	Shape-Based
original_shape_MeshVolume	Shape-Based
original_shape_MinorAxisLength	Shape-Based
original_shape_Sphericity	Shape-Based
original_shape_SurfaceArea	Shape-Based
original_shape_SurfaceVolumeRatio	Shape-Based
original_shape_VoxelVolume	Shape-Based

## References

1. Siegel, R.L., et al., *Cancer statistics, 2023*. *Ca Cancer J Clin*, 2023. **73**(1): p. 17-48.
2. Herbst, R.S., D. Morgensztern, and C. Boshoff, *The biology and management of non-small cell lung cancer*. *Nature*, 2018. **553**(7689): p. 446-454.
3. Knight, S.B., et al., *Progress and prospects of early detection in lung cancer*. *Open Biol*. 2017.
4. Jemal, A. and S.A. Fedewa, *Lung cancer screening with low-dose computed tomography in the United States—2010 to 2015*. *JAMA oncology*, 2017. **3**(9): p. 1278-1281.
5. Armato III, S.G., et al., *The lung image database consortium (LIDC) and image database resource initiative (IDRI): a completed reference database of lung nodules on CT scans*. *Medical physics*, 2011. **38**(2): p. 915-931.
6. Cha, M.J., et al., *Improvement in imaging diagnosis technique and modalities for solitary pulmonary nodules: from ground-glass opacity nodules to part-solid and solid nodules*. *Expert Review of Respiratory Medicine*, 2016. **10**(3): p. 261-278.
7. Swensen, S.J., et al., *Lung nodule enhancement at CT: multicenter study*. *Radiology*, 2000. **214**(1): p. 73-80.
8. Chelala, L., et al., *Lung-RADS version 1.1: challenges and a look ahead, from the AJR special series on radiology reporting and data systems*. *American Journal of Roentgenology*, 2021. **216**(6): p. 1411-1422.
9. Swensen, S.J., et al. *Solitary pulmonary nodules: clinical prediction model versus physicians*. in *Mayo Clinic Proceedings*. 1999. Elsevier.
10. Khan, T., et al., *Diagnosis and management of peripheral lung nodule*. *Annals of Translational Medicine*, 2019. **7**(15).
11. Gillies, R.J., P.E. Kinahan, and H. Hricak, *Radiomics: images are more than pictures, they are data*. *Radiology*, 2016. **278**(2): p. 563-577.
12. Doi, K., *Current status and future potential of computer-aided diagnosis in medical imaging*. *The British journal of radiology*, 2005. **78**(suppl\_1): p. s3-s19.
13. Dey, R., Z. Lu, and Y. Hong. *Diagnostic classification of lung nodules using 3D neural networks*. in *2018 IEEE 15th international symposium on biomedical imaging (ISBI 2018)*. 2018. IEEE.
14. Huang, H., et al., *Self-supervised transfer learning based on domain adaptation for benign-malignant lung nodule classification on thoracic CT*. *IEEE Journal of Biomedical and Health Informatics*, 2022. **26**(8): p. 3860-3871.
15. Kang, G., et al., *3D multi-view convolutional neural networks for lung nodule classification*. *PloS one*, 2017. **12**(11): p. e0188290.
16. Kumar, D., A. Wong, and D.A. Clausi. *Lung nodule classification using deep features in CT images*. in *2015 12th conference on computer and robot vision*. 2015. IEEE.
17. Liu, K. and G. Kang, *Multiview convolutional neural networks for lung nodule classification*. *International Journal of Imaging Systems and Technology*, 2017. **27**(1): p. 12-22.
18. Lu, X., Y.A. Nanekaran, and M. Karimi Fard, *A method for optimal detection of lung cancer based on deep learning optimized by marine predators algorithm*. *Computational Intelligence and Neuroscience*, 2021. **2021**.
19. Mehta, K., et al., *Lung nodule classification using biomarkers, volumetric radiomics, and 3D CNNs*. *Journal of Digital Imaging*, 2021: p. 1-20.
20. Saihood, A., H. Karshenas, and A.R.N. Nilchi, *Deep fusion of gray level co-occurrence matrices for lung nodule classification*. *Plos one*, 2022. **17**(9): p. e0274516.
21. Shen, W., et al. *Multi-scale convolutional neural networks for lung nodule classification*. in *Information Processing in Medical Imaging: 24th International Conference, IPMI 2015, Sabhal Mor Ostaig, Isle of Skye, UK, June 28-July 3, 2015, Proceedings 24*. 2015. Springer.
22. Shen, W., et al., *Multi-crop convolutional neural networks for lung nodule malignancy suspiciousness classification*. *Pattern Recognition*, 2017. **61**: p. 663-673.
23. Tomassini, S., et al., *Lung nodule diagnosis and cancer histology classification from computed tomography data by convolutional neural networks: A survey*. *Computers in Biology and Medicine*, 2022. **146**: p. 105691.
24. Halder, A., S. Chatterjee, and D. Dey, *Adaptive morphology aided 2-pathway convolutional neural network for lung nodule classification*. *Biomedical Signal Processing and Control*, 2022. **72**: p. 103347.
25. Kim, H., et al., *Effect of reconstruction parameters on the quantitative analysis of chest computed tomography*. *Journal of thoracic imaging*, 2019. **34**(2): p. 92-102.
26. Lu, Y., et al., *Investigation of sub-centimeter lung nodule quantification for low-dose PET*. *IEEE Transactions on Radiation and Plasma Medical Sciences*, 2017. **2**(1): p. 41-50.
27. Tonekaboni, S., et al. *What clinicians want: contextualizing explainable machine learning for clinical end use*. in *Machine learning for healthcare conference*. 2019. PMLR.
28. Nioche, C., et al., *LIFEx: a freeware for radiomic feature calculation in multimodality imaging to accelerate advances in the characterization of tumor heterogeneity*. *Cancer research*, 2018. **78**(16): p. 4786-4789.
29. Heeren, T. and R. D'Agostino, *Robustness of the two independent samples t-test when applied to ordinal scaled data*. *Statistics in medicine*, 1987. **6**(1): p. 79-90.
30. Rosner, B., R.J. Glynn, and M.L. Ting Lee, *Incorporation of clustering effects for the Wilcoxon rank sum test: a large-sample approach*. *Biometrics*, 2003. **59**(4): p. 1089-1098.

31. Das, K.R. and A. Imon, *A brief review of tests for normality*. American Journal of Theoretical and Applied Statistics, 2016. **5**(1): p. 5-12.
32. Schultz, B.B., *Levene's test for relative variation*. Systematic Zoology, 1985. **34**(4): p. 449-456.
33. Fonti, V. and E. Belitser, *Feature selection using lasso*. VU Amsterdam research paper in business analytics, 2017. **30**: p. 1-25.
34. Van der Maaten, L. and G. Hinton, *Visualizing data using t-SNE*. Journal of machine learning research, 2008. **9**(11).
35. Suthaharan, S. and S. Suthaharan, *Support vector machine*. Machine learning models and algorithms for big data classification: thinking with examples for effective learning, 2016: p. 207-235.
36. Cervantes, J., et al., *A comprehensive survey on support vector machine classification: Applications, challenges and trends*. Neurocomputing, 2020. **408**: p. 189-215.
37. Frazier, P.I., *A tutorial on Bayesian optimization*. arXiv preprint arXiv:1807.02811, 2018.

**Disclaimer/Publisher's Note:** The statements, opinions and data contained in all publications are solely those of the individual author(s) and contributor(s) and not of MDPI and/or the editor(s). MDPI and/or the editor(s) disclaim responsibility for any injury to people or property resulting from any ideas, methods, instructions or products referred to in the content.